


Article

Hydroxyl Spectroscopy of Laboratory Air Laser-Ignition

Christian G. Parigger^{1,*}, 

¹ Physics and Astronomy Department, University of Tennessee, University of Tennessee Space Institute, Center for Laser Applications, 411 B.H. Goethert Parkway, Tullahoma, TN 37388-9700, USA; cparigge@tennessee.edu

* Correspondence: cparigge@tennessee.edu; Tel.: +1 (931) 841 5690

Abstract: This work investigates spatial and temporal distributions of hydroxyl, OH, in laser-plasma in laboratory air at standard ambient temperature and pressure. Of interest are determination of temperature and density of OH and establishment of a correlation of molecular OH emission spectra with shadow graphs for time delays of 50 to 100 microsecond, analogous to previous work on shadow graph and emission spectroscopy correlation for cyanaide, CN, in gas mixtures and for time delays of the order of 1 microsecond. Wavelength- and sensitivity- corrected spatiotemporal data analysis focuses on temperature inferences using molecular OH emission spectroscopy. Near-ir radiation from a Q-switched laser device initiates optical breakdown in laboratory air. The laser device provides 6 nanosecond, up to 850 milli Joule pulses at a wavelength of 1064 nanometer, and focal irradiance in the range of 1 to 10 Tera Watt per centimeter-squared. Frequency doubled beams are utilized for capturing shadow graphs for visualization of the breakdown kernel at time delays in the range of 0.1 to 100 microsecond. OH emission spectra of the laser plasma, spatially resolved along the slit dimension, are recorded in the wavelength range of 298 nm to 321 nm, and with gate widths adjusted to 10 microsecond for the intensified charge-coupled device that is mounted at the exit plane of a 0.64 m Czerny-Turner configuration spectrometer. Diatomic OH signals occur due to recombination of the plasma and are clearly distinguishable for time delays larger than 50 microsecond, but are masked by spectra of N₂ early in the plasma decay.

Keywords: molecular spectroscopy; diatomic molecules; optical emission spectroscopy; laser induced optical breakdown; hydroxyl; nitrogen second positive; cyanaide; atomic spectroscopy; plasma physics; astrophysics

1. Introduction

Hydroxyl, OH, spectroscopy shows applications in diverse research endeavors including plasma physics, analytical chemistry, astrophysics, and obviously, in combustion physics and associated combustion chemistry [1–6]. The astrophysics OH interest [5] leads to the first hydroxyl radical detection in the near infrared emission spectra of an exoplanet atmosphere. The work presented in this paper is centered on the near-uv spectra of OH in laser-plasma, yet combustion diagnosis of hydrogen flame temperatures in a research rocket combustor may focus on hyperfine structure with experimental resolution of 50 picometer for OH-radical fingerprints [6]. The experimental component initiates laser-plasma [7–10] in standard ambient temperature and pressure (SATP) laboratory air. The analysis component utilizes line strength data that show an accuracy of better than one-thousandth of a nanometer (nm) or 1 picometer (pm) [11] with a typical laser-plasma experiments instrumental resolution of 0.35 nm, or 350 pm [11,12].

The primary reason for occurrence of OH is the presence of moisture in SATP air, however, OH emission signals show spectroscopic interference from the N₂ Second Positive system that usually occurs in nitrogen discharges [13]. Recorded spectra in air breakdown dwarf signal strengths that can be measured in combustion processes that utilize oxygen as oxidizer, for example, combustion of hydrocarbons [14,15]. However, when exploring combustion and laser-plasma in gases, usually strong signals define the spectroscopy of emanating light with notable contributions of diatomic carbon (C₂) Swan bands, cyanide (CN), and atomic signatures of the hydrogen Balmer series, e.g., hydrogen-beta line [16–21]. Laser-plasma in air, and for the wavelength range of 298 nm to 321 nm, reveals significant

contributions from the N₂ Second Positive system of nitrogen at time delays of typically 10 to 30 microsecond after optical breakdown [11,12], and OH emission signals are clearly discernable in the time delay range of 50 μ s to 110 μ s. Spatiotemporal information is obtained by utilizing the slit dimension for the spatial resolution. The temporal resolution is obtained from a systematic set of time delays that are selected for an intensified charge-coupled device (iCCD) mounted at the exit plane of a spectrometer. The experimental methodology including choice of laser-plasma generation by aligning beam propagation and focusing parallel to the slit is analogous to that designed for recent cyanide, CN, diatomic molecular studies [22]. The shadow graphs are recorded by employing a digital camera, thereby allowing one to associate spatial connections with the time-resolved, recorded spectra. The concentration of OH molecules is inferred from equilibrium species distributions computations that employ freely available code for chemical equilibrium with applications [23,24].

2. Materials and Methods

The experimental arrangement for recording of spatiotemporal molecular distributions has been communicated previously, however, for completeness is included in this work. The standard experimental components are used for laser-induced breakdown spectroscopy and have been summarized previously, e.g., see Ref. [11].

The experimental arrangement consists of a set of components typical for time-resolved, laser-induced optical emission spectroscopy, or nanosecond laser-induced breakdown spectroscopy (LIBS). Figure 1 displays the principal schematic of the experimental arrangement.

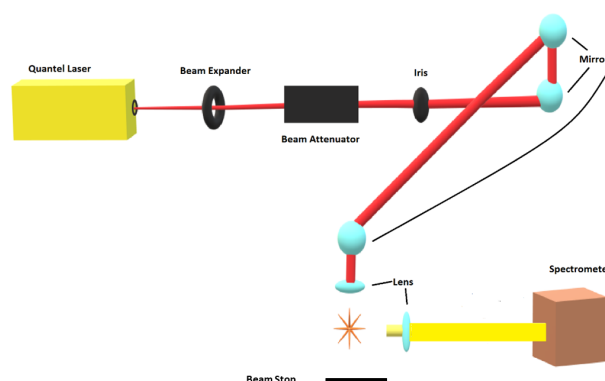


Figure 1. Experimental arrangement for laser-induced breakdown spectroscopy.

Primary instrumentations include a Q-switched Nd:YAG device, Quantel model Q-smart 850, operated at the fundamental wavelength of 1064-nm to produce full-width-at-half-maximum 6-ns laser radiation with an energy of up to 850 mJ per ir pulse, a laboratory type Czerny-Turner spectrometer, Jobin Yvon model HR 640, with a 0.64 m focal length and equipped with a 1200 grooves/mm grating, an intensified charge-coupled device, Andor Technology model iStar DH334T-25U-03, for recording of temporally and spatially resolved spectral data, a laboratory chamber or cell with inlet and outlet ports together with a vacuum system, electronic components for synchronization, and various optical elements for beam shaping, steering and focusing. For 1:1 imaging of the plasma onto the 100 μ m spectrometer slit, a fused silica plano-convex lens, Thorlabs model LA4545, is employed. For the OH experiments, the laser pulse energy is attenuated with beam splitters and apertures from 850 to 170 mJ/pulse. The residual, transmitted laser pulse is captured by the beam stop that is indicated in Fig. 1.

For visualization studies reported here, a separate laser device, Continuum Sure-lite model SL I-10, delivers two frequency-doubled beams at the 2nd harmonic, 532-nm wavelength, and both breakdown and shadowgraph beams are spatially overlapped. The

shadowgraph pulses can be delivered with a minimum time delay of 300 ns and with a well defined time delay showing less than ± 1 ns trigger-jitter between the pulses. Shadowgraphs are recorded by external synchronization of the Surelite and Quantel laser devices and by externally triggering the camera, Silicon Video 9C10 color camera, that records the images that are projected onto a screen. Figure 2 illustrates the modular setup for recording of shadow graphs.

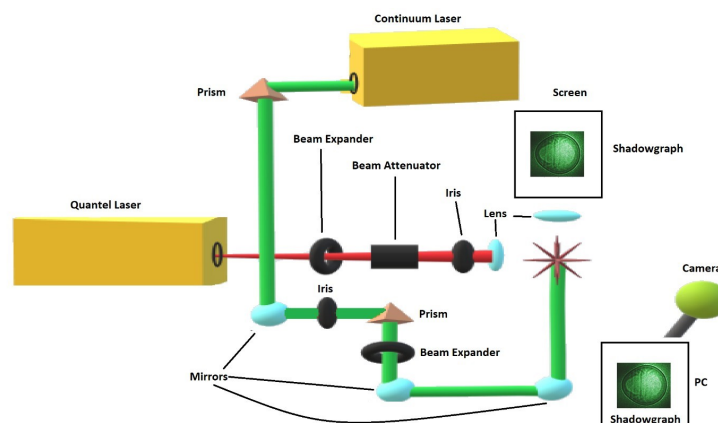


Figure 2. Module for recording shadowgraphs of optical breakdown in air. The collimated Quantel laser beam is focused with $f/20$ optics. The asterisk symbolically indicates optical breakdown. The interaction area is illuminated by time-delayed Continuum Surelite laser beams, and shadows are projected onto a screen and recorded with a digital camera [11].

In studies with time-resolved spectroscopy, optical breakdown was generated at a rate of 10 Hz, with the laser beam focused with $f/5$ optics from the top, or parallel to the slit, analogous to recently reported CN laser spectroscopy [22]. The laser beam, parallel to the slit, arrives from the top (see Fig. 1) and is focused with $f/5$ -optics by an anti-reflection coated, 25.4-mm (1 in.) lens. The air-breakdown plasma is imaged 1:1 with a 50.8-mm lens. Time-resolved data are recorded with an intensified charge-coupled device positioned at the exit plane of the spectrometer.

In the experiments, the irradiance is of the order of $10\times$ more than that needed for optical breakdown in dry air [25]. However, from CO_2 laser breakdown investigations, the breakdown threshold in the moist air troposphere can exceed that of dry air by 20 to 30 percent [26], similar breakdown increase is inferred for 1064-nm Nd:YAG radiation and for 25% humidity during the experimental data collection. The detector pixels are grouped together in 4-pixel tracks along the slit direction, resulting in obtaining 256 spectra for each time delay. Measurements comprise accumulation of 100 consecutive laser-plasma events for 11 separate time delays at $10\ \mu\text{s}$ steps with a $10\ \mu\text{s}$ gate centered at the selected time delay. The selected series explores the plasma decay with specific attention to recognition of OH molecular data that are free from spectroscopic interference. However, the 0-0 OH band edge is marginally recognizable for time delays of $10\ \mu\text{s}$ and $20\ \mu\text{s}$, but almost N_2 interference-free data are captured for time delays as early as about $50\ \mu\text{s}$.

Computation of hydroxyl spectra utilizes well-established line-strength data for the diatomic OH molecule. Application of standard quantum mechanics establishes within the concept of line strengths [27] consistent computation of diatomic spectra. The OH line-strength data are published as a supplement to a recent paper on hydroxyl [11]. However, an abridged data file containing sets of three values, i.e., transition wave numbers, lower-level term values, and transition-strengths, is sufficient for routine computation of diatomic OH spectra using widely available MATLAB software [28] and convenient scripts [29] for computation of spectra and for fitting of recorded spectra.

Figure 3 illustrates computed OH data using the MATLAB BESP.m script [29] for spectral resolutions of 0.001 nm and 0.35 nm, the latter corresponds to a typical resolution in laser-induced spectroscopy with intensified array detectors and the former is used for

nominal pico-meter resolution stick-spectra. OH spectra in the indicated 304 nm to 322 nm wavelength range clearly show the 0-0 band edge near 306 nm of the red shaded $A^2\Sigma^+ \leftrightarrow X^2\Pi_i$ ultraviolet system, the 1-1 band edge is near 312 nm, and the 2-2 band edge near 318 nm [11].

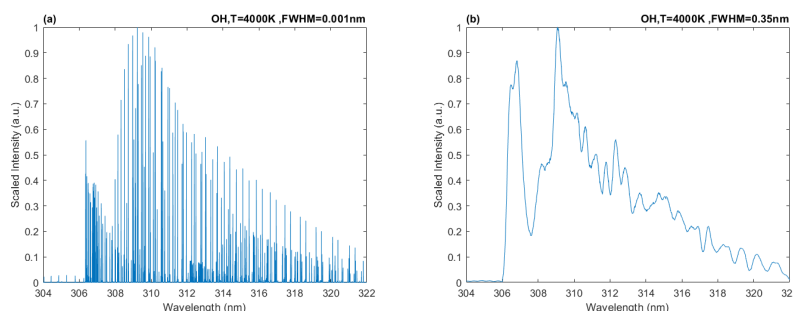


Figure 3. Computed spectra: $T = 4,000$ K; Spectral resolution (a) 0.001 nm and (b) 0.35 nm.

For the OH analysis, the MATLAB NMT.m script [29] was utilized. This particular script allows one to fit measured to computed data employing the Nelder-Mead nonlinear fitting algorithm. As an example, previously measured and communicated data [11,12] are analyzed for determination of temperature using MATLAB. Figure 4 displays the results, consisted with previous temperature inferences [16,17].

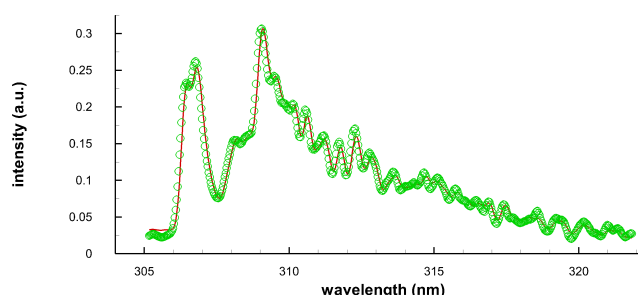


Figure 4. Measured and fitted OH spectra, $T = 3393$ K, spectral resolution: 0.35 nm.

The calculation of the spectra relies on the use of OH line strength data [11]. Computation of diatomic spectra utilizes high resolution data for determination of molecular constants of selected molecular transitions from an upper to a lower energy level. Numerical solutions of the Schrödinger equation for potentials yield r-centroids associated with vibrational transitions usually involving Frank-Condon factors. Calculated rotational factors are interpreted as selection rules because these factors are zero for forbidden transitions, viz. Hönl-London factors.

3. RESULTS AND DISCUSSION

3.1. Shadow Graphs

Investigations of expanding laser-induced shockwaves and fluid-physics phenomena utilize effectively high shutter-speed shadowgraph photography. Figures 5 to 7 display selected shadow graphs for time delays in the range of 0.1 μ s to give-or-take 100 μ s.

The ir laser beam is focused from right to left as indicated by the arrow in the images. The shock wave appears nearly symmetrical for the 1 μ s images, see Fig. 5, that evolved from a spheroidal image captured for time delays of 0.1 μ s. In the 0.1 to 1 μ s range, CN recombination spectra are measured [22]. The species density increase of electrons and diatomic molecular CN near the shockwave can be determined using Abel integral inversion [22].

Figures 6 and 7 illustrate selected shadowgraphs for time delays of 54.25 μ s and 104.25 μ s, respectively. Well developed vortices and fluid flow occurs towards the incom-

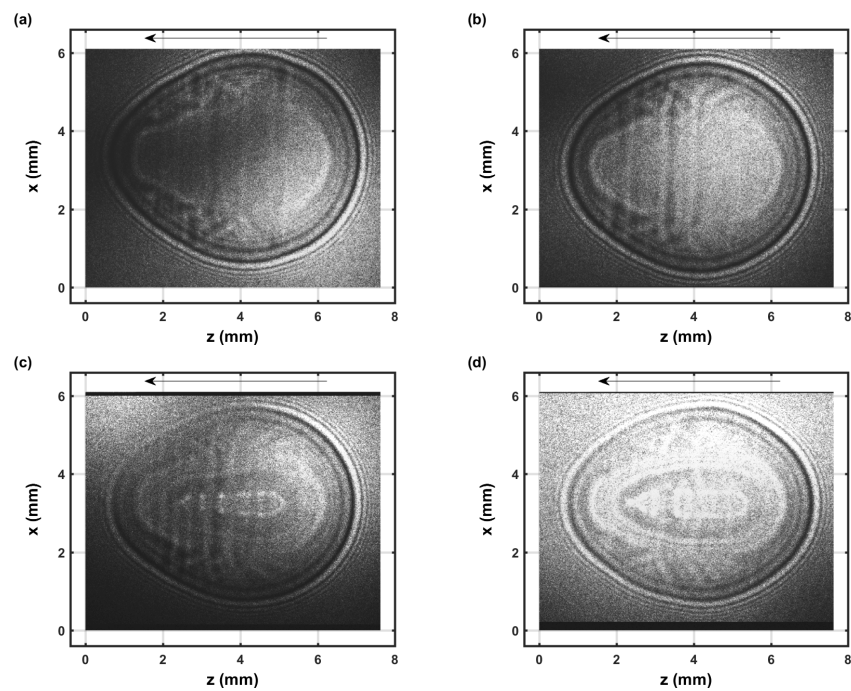


Figure 5. Single-shot shadowgraph of the expanding laser-induced plasma initiated with a 170-mJ, 6-ns, 1064-nm focused beam, and imaged using a 5-ns, 532-nm back-light that is time-delayed by 1 μ s (a) and (b). Double images for time delays of 1 μ s and 0.1 μ s (c) and (d).

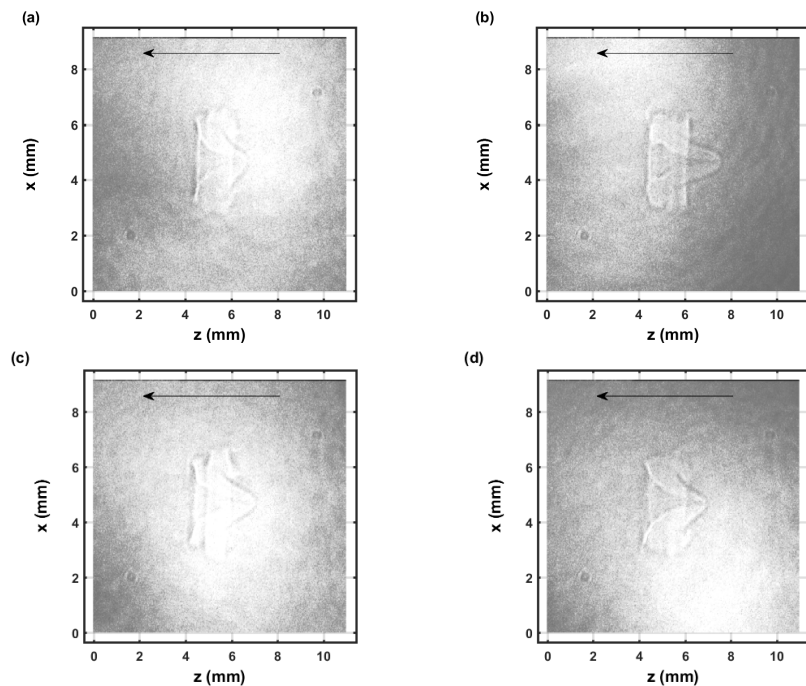


Figure 6. Single-shot shadowgraph of the expanding laser-induced plasma initiated with a 170-mJ, 6-ns, 1064-nm focused beam, and imaged using a 5-ns, 532-nm back-light that is time-delayed by 54.25 μ s (a),(b),(c), and (d) display images from separate laser pulses.

ing laser beam. The captured images for 54.25- μ s time delays (Fig. 6) appear to show slightly more apparent variations than those for 104.25- μ s time delays (Fig. 7). However, spatial variations are not obvious in the measured spatiotemporal OH spectra that are communicated in the next section.

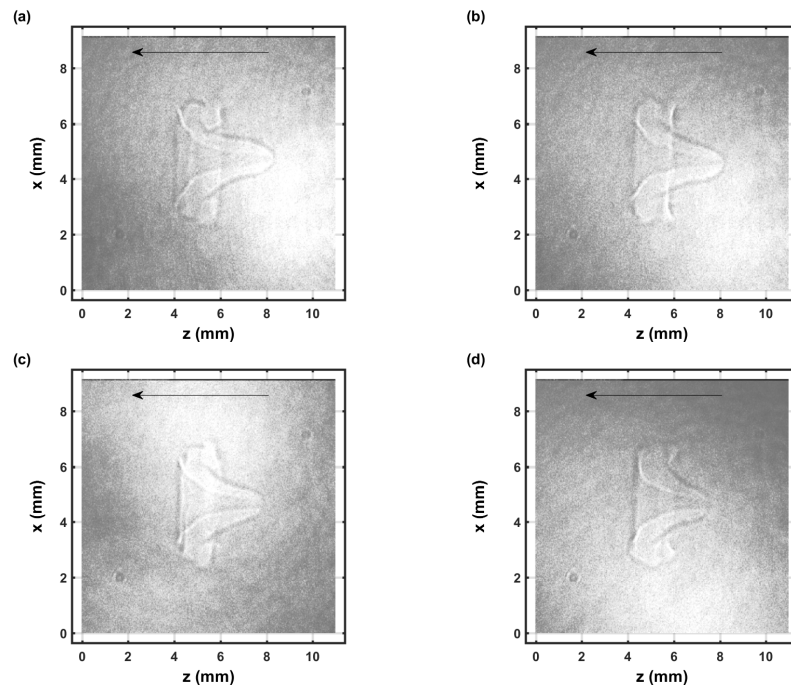


Figure 7. Single-shot shadowgraph of the expanding laser-induced plasma initiated with a 170-mJ, 6-ns, 1064-nm focused beam, and imaged using a 5-ns, 532-nm back-light that is time-delayed by 104.25 μ s (a),(b),(c), and (d) display images from separate laser pulses.

In view of laser spectroscopy, time-resolved data taken for a narrow slice along the direction of the laser beam would be affected by fluid dynamics. By comparison, Fig. 5 indicates close to spherical symmetry allowing one to utilize Abel inverse transform algorithms [22]. Spectroscopic diagnosis and correlation with the shadowgraphs of Figs. 6 and 7 is expected to require simultaneous measurements in multiple or at least two directions, in other words, desirable is a computed tomography approach that utilizes Radon inverse transform. For the employed experimental arrangement, integration occurs along the line-of-sight causing ambiguities in inferences of densities for obviously non-spherical expansion. However, the overall fluid expansion has been measured and computed previously in combustion research along with experimental studies utilizing planar laser-induced fluorescence [14,15].

3.2. Emission Spectra

Figures 8, 9, and 10 illustrate recorded emission spectra along the slit height and in the range of 304 nm to 321.3 nm, and for time delays of 10 μ s to 110 μ s in 10 μ s steps. All images are individually scaled from minimum to maximum and processed for pseudo-color display.

The intensified detector has the capability of recording 1024 spatially resolved data, however, 4 vertical pixels are grouped together for increased sensitivity of the actually recorded 256 spectra. The figures illustrate reasonable integrated signals from 100 consecutive laser-plasma events that are dispersed in approximately 100 spectra in the central region of the detector. Fig. 8 (a) displays faint N_2 Second Positive band-edge signals near 315 nm, but Fig. 8 (b) reveals the OH A-X 0-0 band edge near 306 nm together with well demarcated N_2 signals. Figs. 8 (c) and (d) depict how N_2 signals diminish as OH becomes apparent.

Experimental averaging over 100 consecutive laser-plasma events enhances the signal to noise ratio by one order of magnitude. Conversely, as one collapses the 1024 vertical pixels to a single super-pixel, one mimics a linear diode array capable of recording single-

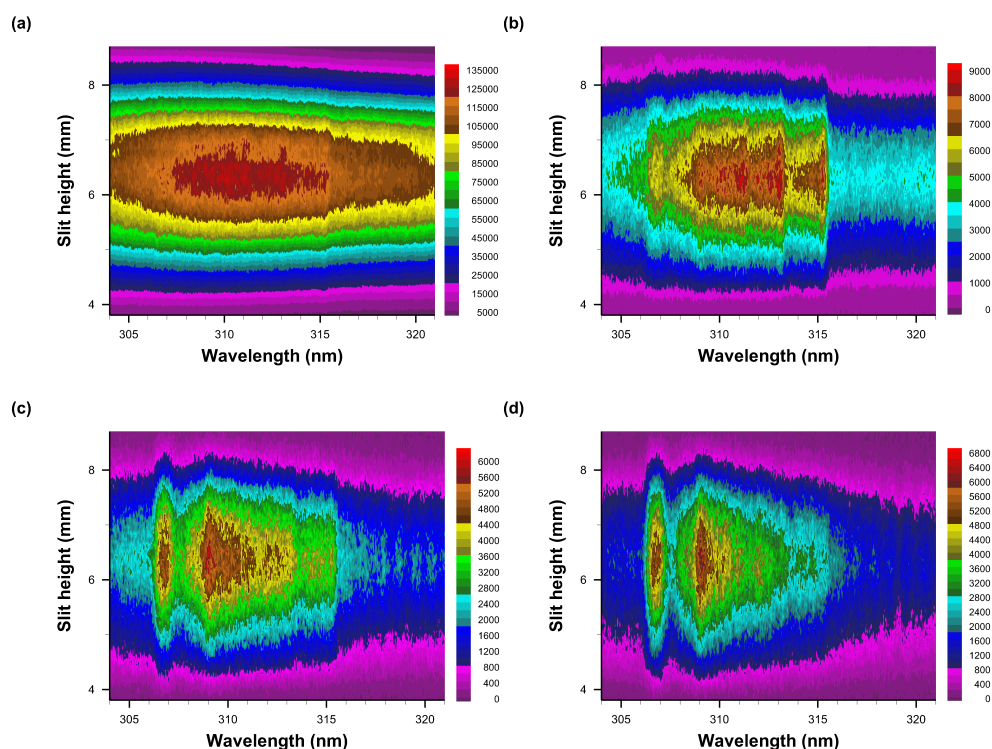


Figure 8. Recorded data of slit-height vs. wavelength. Gate width: 10 μ s, time delay (a) 10 μ s – primarily N₂ second positive spectra, (b) 20 μ s, (c) 30 μ s, and (d) 40 μ s. The A-X 0-0 band edge is identified in figure (b). Each pseudo-colored image is scaled from minimum to maximum.

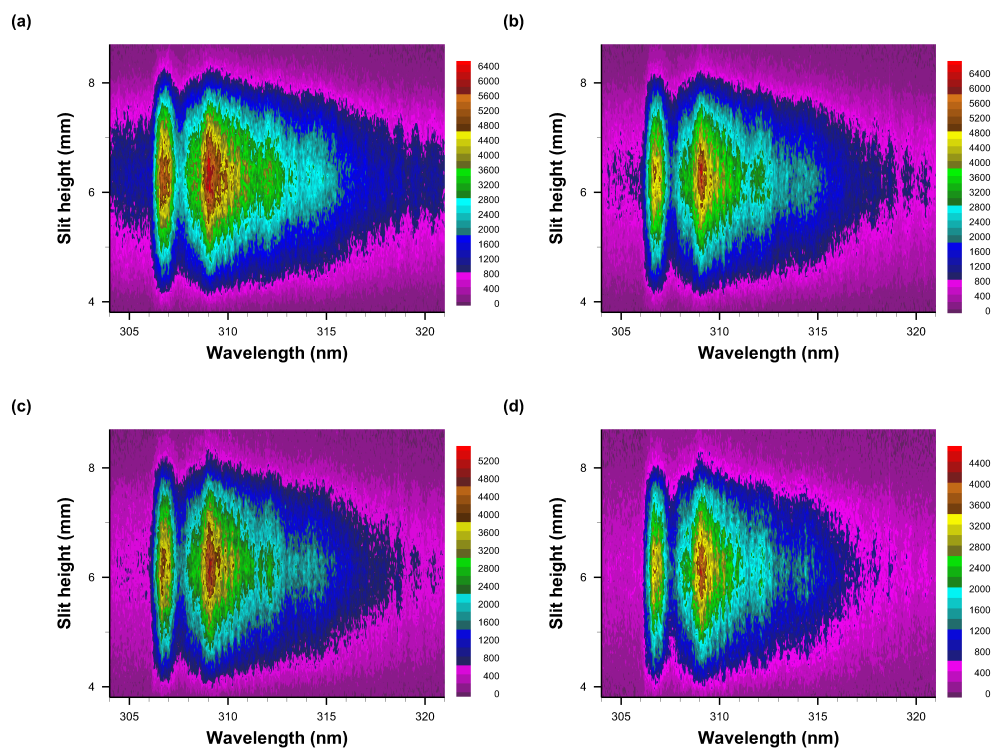


Figure 9. Recorded data of slit-height vs. wavelength. Gate width: 10 μ s, time delay (a) 50 μ s – primarily OH spectra, (b) 60 μ s, (c) 70 μ s, and (d) 80 μ s. Each pseudo-colored image is scaled from minimum to maximum.

shot OH spectra in laboratory air. Inspection of the spectra reveals that there is a slight curvature that would cause decreased resolution when averaging the central spectra.

Figures 9 (a) and (b) indicate similar, OH-band integrated signals or close to maximum OH signals as function of temperature if one computes the equilibrium species density v . temperature [11] and for a measured level of humidity. For air with 25% relative humidity, the OH density reaches a maximum of $\simeq 3 \times 10^{16} \text{ cm}^{-3}$ at a temperature of $T \simeq 3100 \text{ K}$.

Figure 10 illustrates the persistence of OH emission spectra for time delays of 90 μs to 110 μs , including two resolved peaks near the A-X 0-0 OH band edge that can be seen for an experimental spectral resolution of 0.35 nm.

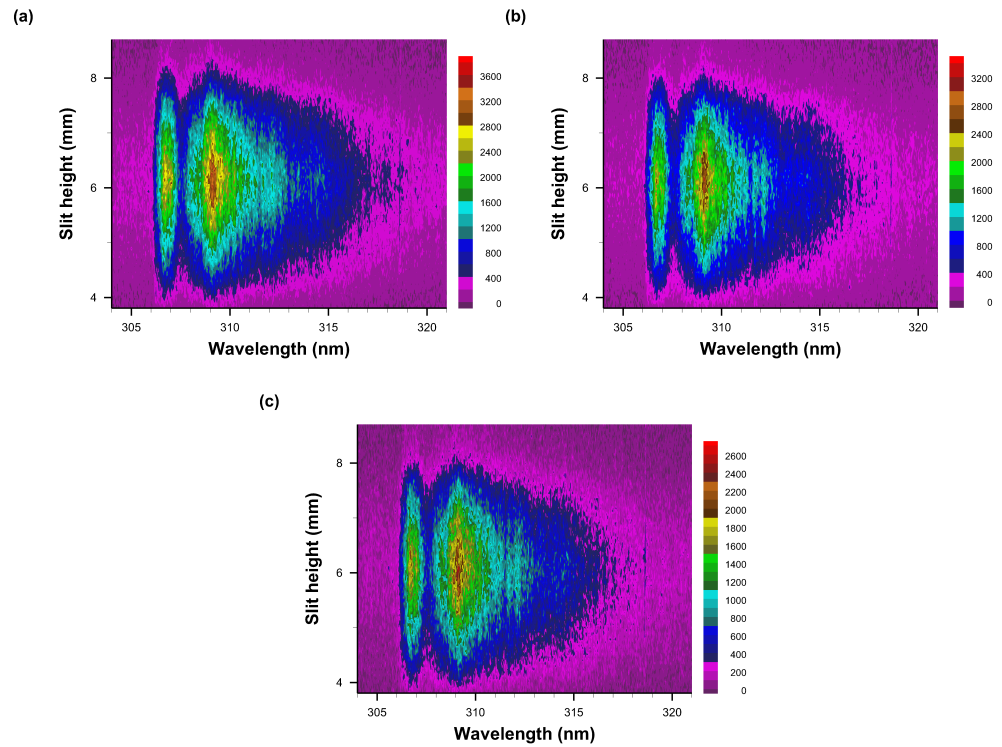


Figure 10. Recorded data of slit-height vs. wavelength. Gate width: 10 μs , time delay (a) 90 μs , (b) 100 μs , and (c) 110 μs . Each pseudo-colored image is scaled from minimum to maximum.

Measurement of OH in moisture-laden laboratory air can be accomplished at the single-shot level as elaborated above, i.e., when grouping together all vertical bins, thereby simulating a linear diode array. Figures 11 to 13 display averages of the 5.44 mm central portion of the spatiotemporal data in Figs. 8 to 10.

Figure 14 illustrates inferred temperatures from averages of wavelength calibrated and sensitivity corrected data in Figs. 11 to 13 of the displayed images in Figs. 8 to 10. The fitting procedures uses the Nelder-Mead algorithm and OH line-strength data for spectra fitting with constant instrument resolution of 0.35 nm and allowing a straight line background correction as well. The quoted instrument resolution is associated with the center wavelength of the displayed data. OH line strength data are utilized in terms of transition and lower term value wave-numbers that are adjusted to air wavelengths in the fitting program. For the 10-microsecond time-delay data, the temperature is estimated to be 1 eV, or 11,600 K, guided by Wien's displacement law [30],

$$\lambda_{\text{peak}} = b/T. \quad (1)$$

Wien's displacement constant equals, $b = 2.897 \times 10^{-3} \text{ m K}$, λ_{peak} indicates the peak of the spectral radiance of black-body radiation, and T is the absolute temperature.

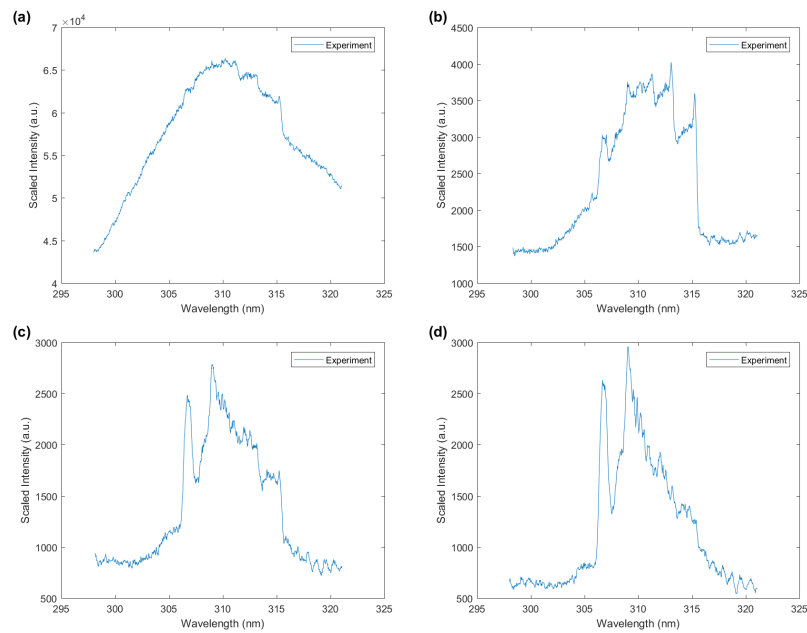


Figure 11. Wavelength calibrated and sensitivity corrected data of vertical average vs. wavelength. The OH A-X 0-0 band edge near 306 nm is the initial indicator of presence of the hydroxyl radical. Gate width: 10 μ s, time delay (a) 10 μ s – OH and N₂ second positive barely developed (b) 20 μ s – primarily N₂ second positive spectra, (c) 30 μ s, and (d) 40 μ s – primarily OH uv A-X spectra.

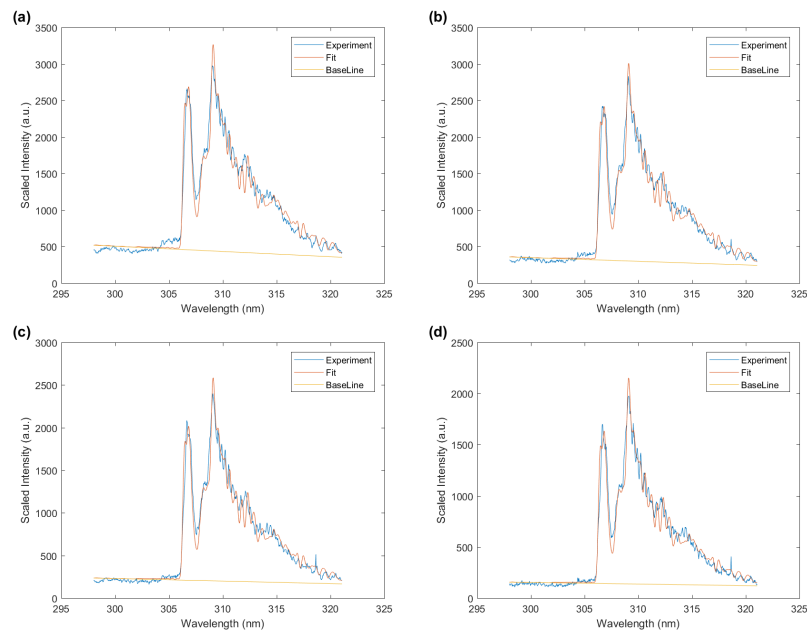


Figure 12. Wavelength calibrated and sensitivity corrected data of vertical average vs. wavelength, fitted data with spectral resolution of 0.35 nm, and baseline. Gate width: 10 μ s, time delay (a) 50 μ s, T = 3290 K, (b) 60 μ s, T = 3190 K (c) 70 μ s, T = 3050 K, and (d) 80 μ s, T = 2930 K.

The double exponential fit, Figure 14, utilizes the MATLAB fit.m function to parameters a , b_1 , c_1 , b_2 , c_2 for the function $f(x) = a + b_1 * \exp(-c_1 * x) + b_2 * \exp(-c_2 * x)$. The fitting routine finds the respective values of 2.14, 31.7, 0.146, 2.41, 0.0144, when using kK and μ s units in the fitting routine. From Figure 10 (a), one would infer from Eq. (1) a temperature of 9350 K. However, diatomic spectra of OH and N₂ second positive are already developed. Consequently, the temperature is estimated to be higher than indicated by the peak in the 10- μ s average data. Temperatures for the 20 μ s to 110 μ s data range are

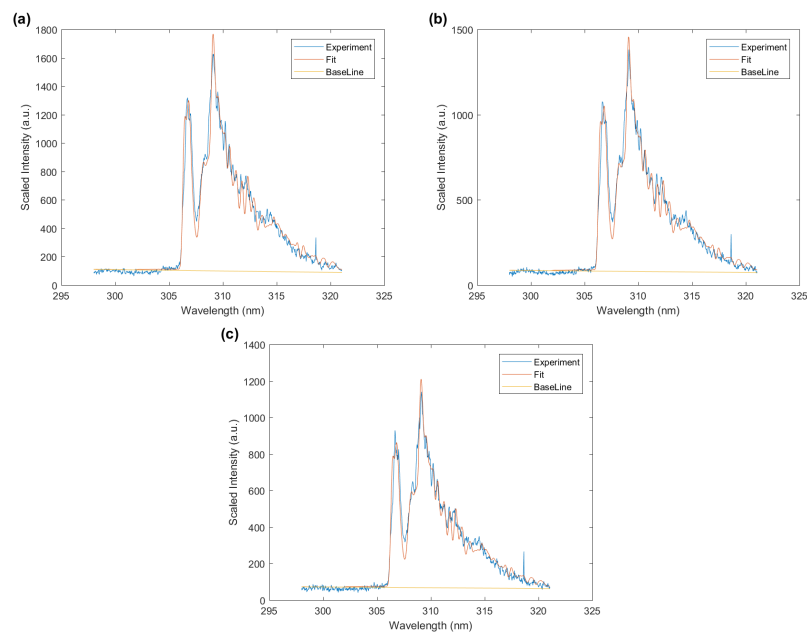


Figure 13. Wavelength calibrated and sensitivity corrected data of vertical average vs. wavelength, fitted data with spectral resolution of 0.35 nm, and baseline. Gate width: 10 μs , time delay (a) 90 μs , T = 2780 K (b) 100 μs , T = 2690 K, and (c) 110 μs , T = 2640 K.

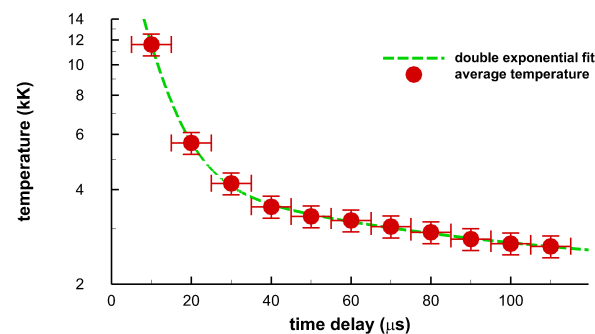


Figure 14. Inferred temperature from spatial averages of the displayed images for 10 μs to 110 μs . The dashed line indicates a double exponential fit to the data, see text.

inferred from only fitting OH. The temperature error bars indicate a range of ± 8 percent, and the horizontal error bars indicate the gate-width of 10 μs .

3.3. Correlation of OH Emission Spectra and of Shadow Graphs

The recorded optical emission data of OH are difficult to connect with the measured shadow graphs [11]. However, expansive analysis of spatiotemporal data allows one to establish initial connections. First, average temperatures are associated with the equilibrium OH density for the spatiotemporal data, and second, spatially resolved temperatures are associated with OH density variations indicated in the shadow graphs.

The equilibrium OH concentrations are computed from the mole fraction data for the experiments in SATP laboratory air. The CEA program computes a volley of species for equilibrium conditions. Table 1 shows all species for selected temperatures in the range of 2500 K and 3750 K. The OH mole fraction peaks at 3144 K, and the OH mole fraction ratio at 6000 K and at 3100 K would amount to 3.6×10^{-3} .

Table 1: Mole fractions for $T = 2500$ K, $T = 3100$ K, and $T = 3750$ K, from computation of air species with the CEA-program, and for 25% relative humidity.

species	mole fraction for 2500 K	mole fraction for 3100 K	mole fraction for 3750 K
e^-	4.147×10^{-10}	4.916×10^{-8}	1.3111×10^{-6}
Ar	9.1983×10^{-3}	8.9044×10^{-3}	8.1562×10^{-3}
H	2.7114×10^{-4}	4.4885×10^{-3}	1.3839×10^{-2}
H^+	-	-	1.585×10^{-12}
H^-	-	-	1.653×10^{-10}
HNO	9.4651×10^{-8}	4.3791×10^{-7}	3.7013×10^{-7}
HNO_2	8.4537×10^{-8}	6.3610×10^{-8}	9.598×10^{-9}
HO_2	4.0794×10^{-6}	6.6671×10^{-6}	1.8016×10^{-6}
H_2	1.1744×10^{-4}	4.5033×10^{-4}	1.9256×10^{-4}
H_2O	8.7192×10^{-3}	2.8062×10^{-3}	1.3692×10^{-4}
H_2O_2	2.7318×10^{-8}	2.1904×10^{-8}	1.424×10^{-9}
N	2.524×10^{-7}	2.192×10^{-5}	5.4050×10^{-4}
N^+	-	-	1.489×10^{-14}
N^-	-	-	2.236×10^{-12}
NH	3.634×10^{-9}	1.943×10^{-7}	1.3517×10^{-6}
NH_2	1.103×10^{-10}	2.329×10^{-9}	3.358×10^{-9}
NO	2.1548×10^{-2}	4.3043×10^{-2}	4.6896×10^{-2}
NO^+	4.410×10^{-10}	5.107×10^{-8}	1.3420×10^{-6}
NO_2	1.8594×10^{-5}	1.9773×10^{-5}	9.4889×10^{-6}
N_2	7.5738×10^{-1}	7.2208×10^{-1}	6.5741×10^{-1}
N_2^-	-	-	7.627×10^{-13}
N_2^+	-	-	5.901×10^{-11}
N_2O	1.1849×10^{-6}	2.3699×10^{-6}	2.5855×10^{-6}
N_3	-	-	2.874×10^{-10}
O	6.3014×10^{-3}	6.0120×10^{-2}	2.1044×10^{-1}
O^+	-	-	2.075×10^{-11}
O^-	7.548×10^{-12}	1.339×10^{-9}	3.0021×10^{-8}
OH	4.5941×10^{-3}	1.0814×10^{-2}	5.4876×10^{-3}
O_2	1.918×10^{-1}	1.4724×10^{-1}	5.6886×10^{-2}
O_2^+	-	-	1.346×10^{-9}
O_2^-	-	-	1.124×10^{-9}
O_3	3.0933×10^{-8}	9.5514×10^{-8}	7.9000×10^{-8}

Figure 15 displays equilibrium OH density versus temperature for the majority of the time-delays selected in the experiment.

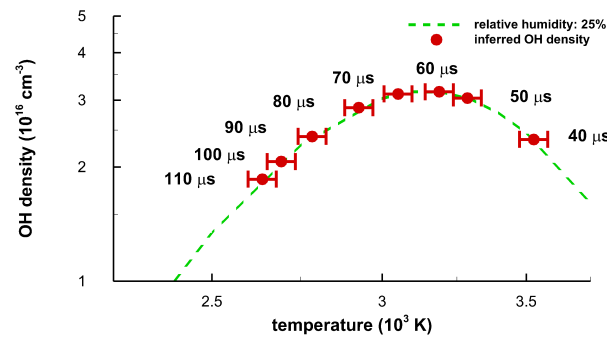


Figure 15. Equilibrium density of OH versus average temperature for a relative humidity of 25 per cent. The data points correspond to the indicated time delays. The error bars indicate ± 1.5 per cent variation. Maximum OH density of $3.17 \times 10^{16} \text{ cm}^{-3}$ occurs at a temperature of 3.144 K.

Analysis of the 1100 spectra in the central region of the 2816 captured spatially- and temporally- resolved data reveals subtle differences along the plasma, i.e., along the spectrometer slit dimension. For the time delays of 50 μs and 100 μs , Figure 16 displays temperature vs slit height. Near 4 mm and 6 mm, there appear to be lower OH concentrations, corresponding to the toroid in the center of Figs. 6 and 7. In turn, in the other regions, OH concentrations appear higher than near the toroid edges as the temperatures are closer to the maximum OH concentration line at 3144 K for 25% relative humidity. Furthermore, OH concentration appears to be elevated towards 9 mm, but comparable to those in the central region. A slight OH concentration increase towards the top of the slit, or towards the incoming laser beam and especially for the 100 μs -data, may be indicative of the apparent fluid-dynamic expansion towards the incoming beam. The fluid dynamics expansion can be seen in shadow graphs and are illustrated for time delays of 50 μs and

100 μ s, see Figs. 6 and 7. The variation of individual results is expected due to the collection of spatiotemporal spectra for 100 breakdown events and for each time delay.

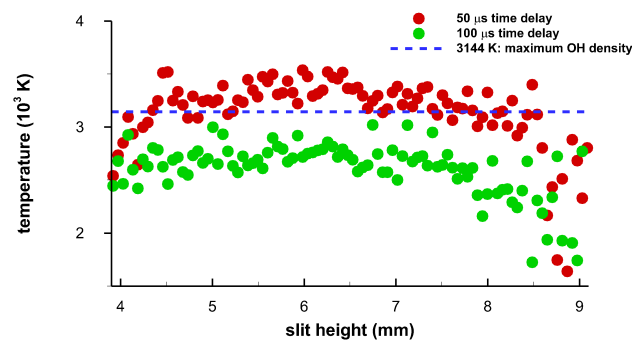


Figure 16. Temperature versus slit height for time delays of 50 μ s and 100 μ s. The horizontal dotted line indicates the temperature of 3144 K at which the OH density maximizes to $3.17 \times 10^{16} \text{cm}^{-3}$.

The individual data points in Figure 16 are obtained by fitting the captured data to computed OH spectra. Fig. 17 illustrates the results for time delays of 50 μ s and 100 μ s at the the slit height of 6.43 mm.

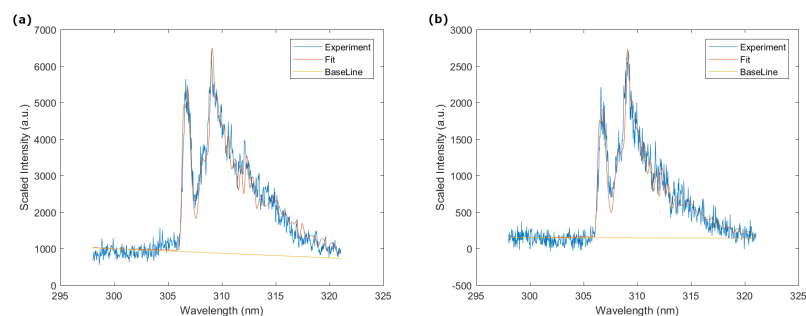


Figure 17. Spectrum fitting results for slit height of 6.43 mm and spectral resolution of 0.35 nm . (a) $T = 3374$ K, time delay 50 μ s, (b) $T = 2580$ K, time delay 100 μ s.

In combustion investigation of for example hydrocarbon laser ignition, OH signals are significantly larger than those obtained in laboratory air breakdown. However, planar laser induced fluorescence, or planar LIF, is usually applied in laser-initiated combustion that allows one to correlate shadowgraphs with fluid physics expansion of the kernel [14,15]. However, spectra of CN that are recorded within the first microsecond after initiation of laser plasma in laboratory can be associated with the expanding shock wave [22]. An increase in electron density is inferred near the shockwave from analysis of a carbon atomic line superposed with the CN emission spectrum, and Abel inversion techniques allows one to associate increased CN density near the expanding shock wave.

4. CONCLUSIONS

A correlation of spatially- and temporally- resolved OH emission spectra and of shadow graphs is challenging. OH signals are discernible early in the laser-plasma and appear spectrally interference-free at time delays of typically 50 microsecond after optical air breakdown. For time delays of the order of 50 to 100 microsecond, fluid physics phenomena become apparent and appear cylindrically symmetric, but the laser-plasma kernel can not be modeled as spherically symmetry. For time delays of 1 microsecond, the shock wave appears spherically symmetric allowing one to utilize Abel inverse integral techniques to determine the spatial electron density and diatomic molecular CN distribution. However, when utilizing chemical equilibrium distribution predictions for moisture laden air, one can associate shadow graphs that are captured for time delays of typically 50 μ s and 100 μ s with

corresponding spatiotemporally resolved OH emission. From the fitted OH temperature one can infer OH densities of $\sim 3 \times 10^{16} \text{ cm}^{-3}$ for 25 % relative humidity laboratory air, and slight density variations that are associated with optical-breakdown-kernel fluid dynamic expansion for time delays of the order of 100 μs .

Acknowledgments: The author acknowledges support in part the State of Tennessee funded Center for Laser Applications at the University of Tennessee Space Institute.

Funding: This research received no specific grant-number external funding.

Acknowledgments: The author acknowledges support in part the State of Tennessee funded Center for Laser Applications at the University of Tennessee Space Institute.

Conflicts of Interest: The author declares no conflict of interest. The funders had no role in the design of the study; in the collection, analyses, or interpretation of data; in the writing of the manuscript, or in the decision to publish the results.

Abbreviations

The following abbreviations are used in this manuscript:

CN	Cyanide
BESP	Boltzmann Equilibrium Spectrum Program
iCCD	intensified Charge-Coupled Device
LIBS	Laser-Induced Breakdown Spectroscopy
Nd:YAG	Neodymium-doped Yttrium Aluminium Garnet
NMT	Nelder-Mead Temperature
OH	Hydroxyl
SATP	Standard Ambient Temperature Pressure

References

1. Kunze, H.-J. Introduction to Plasma Spectroscopy, Springer, Heidelberg, GER, 2009.
2. Fujimoto, T. Plasma Spectroscopy, Clarendon Press, Oxford, UK, 2004.
3. Ochkin, V.N. Spectroscopy of Low Temperature Plasma, Wiley-VCH, Weinheim, GER, 2009.
4. Boulos, M.I.; Fauchais, P.; Pfender E. Thermal Plasmas. Fundamentals and Applications, Plenum Press, London, UK, 1994.
5. Nugroho, S.K.; Kawahara, H.; Gibson, N. P.; de Mooij, E.J.W.; Hirano, T.; Kotani, T.; Kawashima, Y.; Masuda, K.; Brogi, M.; Birkby, J.L.; Watson, C.A.; Tamura, M.; Zwintz, K.; Harakawa, H.; Kudo, T.; Kuzuhara, M.; Hodapp, K.; Ishizuka, M.; Jacobson, S.; Konishi, M.; Kurokawa, T.; Nishikawa, J.; Omiya, M.; Serizawa, T.; Ueda, A.; Vievard, S. *Astrophys. J. Lett.* 910, 2021, L9, 9 pp.
6. Stützer, R.; Oschwald, M. *8th European Conference for Aeronautics and Space Sciences (EUCASS) 2019*, 2019-839, 8 pp.
7. Radziemski, L.J.; Cremers, D. A., Eds. Laser-Induced Plasmas and Applications, Dekker: New York, NY, USA, 1989.
8. Miziolek, A.W., Palleschi, V., Schechter, I., Eds. Laser Induced Breakdown Spectroscopy (LIBS): Fundamentals and Applications, Cambridge Univ. Press: New York, NY, USA, 2006.
9. J.P. Singh; S.N. Thakur, Eds. Molecular Laser-Induced Breakdown Spectroscopy, Laser Induced Breakdown Spectroscopy, 2nd Ed., Elsevier: New York, Amsterdam, NL, 2020.
10. De Giacomo, A.; Hermann, J. J. *Phys. D: Appl. Phys* 2017, 50, 183002, 17 pp.
11. Parigger, C.G.; Helstern, C.M.; Jordan, B.S.; Surmick, D.M.; Splinter, R. *Molecules* 25, 2020, 988, 18 pp.
12. Parigger, C.G. *Int. Rev. At. Mol. Phys* 13, 2022, 15–25.
13. Fatima, H.; Ullah, M. U.; Ahmad, S.; Imran, M.; Sajjad, S.; Hussain, S.; Qayyum, A. *SN Applied Sciences* 3, 2021, 646, 12 pp.
14. Chen Y.-L.; Lewis, J.W.L. *Opt. Express* 2001, 9, 360–372.
15. Qin, W.; Chen, Y.-L.; Lewis, J.W.L. *International Flame Research Foundation (IFRF) Combust. J.* 2005, ISSN: 1562-479X, 200508.
16. Parigger, C.G.; Guan, G.; Hornkohl, J.O. *Appl. Opt.* 2003, 42, 5986–5991.
17. Parigger, C.G. Laser-induced breakdown in gases: Experiments and simulation. In *Laser Induced Breakdown Spectroscopy (LIBS): Fundamentals and Applications*; Miziolek, A.W., Palleschi, V., Schechter, I., Eds.; Cambridge Univ. Press: New York, NY, USA, 2006; Chap. 4, pp. 171–193.
18. Parigger, C.G.; Surmick, D.M.; Helstern, C.M.; Gautam G.; Bol'shakov, A.A.; R. Russo. Molecular Laser-Induced Breakdown Spectroscopy, In *Laser Induced Breakdown Spectroscopy, 2nd Ed.*; J.P. Singh, S.N. Thakur, Eds.; Elsevier New York, Amsterdam, NL, 2020; Chap. 7, pp. 167–212.
19. Parigger, C.G.; Hornkohl, J.O. *Quantum Mechanics of the Diatomic Molecule with Applications*; IOP Publishing: Bristol, UK, 2020.
20. Parigger, C.G.; Woods, A.C.; Surmick, D.M.; Gautam, G.; Witte, M.J.; Hornkohl, J.O. *Spectrochim. Acta Part B At. Spectrosc.* 2015, 107, 132–138.
21. Parigger, C.G. *Spectrochim. Acta Part B At. Spectrosc.* 2021, 179, 106122, 12 pp.

-
22. Parigger, C.G.; Helstern, C.M.; Jordan, B.S.; Surmick, D.M.; Splinter, R. *Molecules* **25**, 2020, 615, 13 pp.
 23. Gordon, S.; McBride, B. Computer program for calculation of complex equilibrium compositions, rocket performance, incident and reflected shocks, and Chapman-Jouguet detonations, NASA Lewis Research Center, Interim Revision, NASA Report SP-273 (1976).
 24. McBride, B.J.; S. Gordon. Computer Program for Calculating and Fitting Thermodynamic Functions, NASA RP-1271, 1992; on-line 2005 version, <https://cearun.grc.nasa.gov/> (accessed December 14, 2019).
 25. Thiyagarajan, M.; Thompson, S. J. *Appl. Phys* **111**, 2012, 073302, 8 pp.
 26. Budnik, A.P.; Vakulovskii, A.S. *Atmospheric optics (A91-29962 11-46): Moscow, Gidrometeoizdat*, 1990, 33–37. In Russian.
 27. Condon, E.U.; Shortley, G. *The Theory of Atomic Spectra*; Cambridge University Press: Cambridge, UK, 1953.
 28. MATLAB Release R2022a Update 5, The MathWorks, Inc., Natick, Massachusetts, US, 12 August 2022,
 29. Surmick, D.M.; Hornkohl, J.O. Private communication, The University of Tennessee, University of Tennessee Space Institute, Tullahoma, Tennessee, US, 25 April 2016.
 30. Hertel, I.V.; Schulz C.-P. *Atoms, Molecules and Optical Physics 1, Atoms and Spectroscopy*; Springer: Heidelberg, DE, 2015.